

ARTICLE OPEN



Microbiologically influenced corrosion inhibition of carbon steel via biomineralization induced by *Shewanella putrefaciens*

Yuntian Lou^{1,2,4}, Weiwei Chang^{1,2,4}, Tianyu Cui^{1,2}, Hongchang Qian^{1,2,3}, Luyao Huang^{1,2}, Lingwei Ma^{1,2,3}, Xiangping Hao^{1,2,3} and Dawei Zhang^{1,2,3} 

Microbiologically influenced corrosion inhibition (MICI) of Q235 carbon steel by biomineralization was investigated via a combination of surface analysis, electrochemistry, and scanning electrochemical microscopy (SECM). The results showed that *Shewanella putrefaciens* used the cell walls as the nucleation sites to induce the formation of a protective biomineralized layers which contained calcite and extracellular polymeric substances on the steel surface. The potentiodynamic polarization results demonstrated that the corrosion current density (i_{corr} value) of the biomineralized steel surface was $0.38 \mu\text{A cm}^{-2}$, which was less than one-tenth that of the blank steel in a sterile medium ($4.86 \mu\text{A cm}^{-2}$) after 14 days. The biomineralized layers presented wear resistance and could self-repair after undergoing mechanical damage under microbial conditions as verified by morphological and SECM observations. This work reveals that microbial-induced carbonate biomineralization, as a MICI approach, may be considered as a reliable, low-cost, environmentally friendly corrosion inhibition strategy.

npj Materials Degradation (2021)5:59; <https://doi.org/10.1038/s41529-021-00206-0>

INTRODUCTION

Corrosion is the result of spontaneous chemical or electrochemical reactions between metals and the surrounding environment and has costly and detrimental effects on a variety of industries^{1,2}. To achieve corrosion protection, corrosion-resistant alloys, organic coatings, corrosion inhibitors, and anodic/cathodic protection are widely used, but the limitations of these materials, such as high cost, heavy contamination, and operational difficulties, have not been completely overcome^{3–6}. As a result of in-depth research on metal products that were preserved over a dozen centuries ago via archeological processes and metallic materials that were slightly degraded in renovation projects, it was found that microorganisms may play a key role in inhibiting corrosion^{7,8}. Based on the above studies, microbiologically influenced corrosion inhibition (MICI), as an environmentally friendly anticorrosion method, is expected to be adopted as a green anticorrosion strategy in the future^{9–11}.

MICI directly or indirectly mitigates corrosion through microorganisms and their metabolic activities, such as microbial respiration to consume corrosive substances, formation of an extracellular polymeric substance (EPS) protective layer, formation of a microbiologically induced mineralized layer, competitive microbial corrosion inhibition, and secretion of corrosion inhibitors¹². Due to the complexity of the environment and the diversity of microorganisms, multiple MICI mechanisms may coexist and synergistically inhibit corrosion. For example, Faisal et al.¹³ discovered that *Shewanella oneidensis* sp., a facultative anaerobic iron-reducing bacterium (IRB), could inhibit corrosion of X52 carbon steel through aerobic respiration and iron respiration. After repeated redox deposition of iron and mixing with EPSs, a dense protective layer was formed on the metal surface, resulting in a maximum corrosion rate of only $\sim 0.1 \text{ mm y}^{-1}$ in an *S. oneidensis*-inoculated medium and $\sim 0.5 \text{ mm y}^{-1}$ in a sterile medium. Nardy

et al.¹⁴ discovered the formation of mineral deposition layers on the surface of sheet piling used for reinforcement of waterways and dikes, which did not suffer serious corrosion even after over 50 years of use. According to microbial community analysis, the formation of mineral deposition layers was closely related to the metabolic processes of methanogens¹⁵.

As an MICI mechanism, microbiologically induced carbonate precipitation (MICP) has been applied for corrosion protection and repair of concretes^{16–21}. MICP refers to the use of microbial cell walls or EPSs as crystal nucleation sites to form a microenvironment with high concentrations of carbonate and calcium ions, thereby promoting the deposition of carbonates^{22–25}. Due to differences in the metabolic characteristics of microorganisms, the morphology of calcium carbonate can vary, with forms such as calcite, aragonite, and vaterite, among which calcite is the most stable crystal structure^{26,27}. Xu et al.²⁸ investigated the potential of *Sporosarcina pasteurii* DSM 33 immobilized in porous ceramic particles to be used as a self-healing agent for the repair of cracks in reinforced concrete. Microorganism intervention promoted the complete healing of the cracks within 120 days, with a maximum repair width of $450 \mu\text{m}$. The Tafel polarization results indicated that the concrete underwent active-to-passive transitions during the MICP process. However, MICP for corrosion protection of metallic materials has been developing in recent years. Liu et al.²⁹ found that marine *Pseudoalteromonas lipolytica* could convert biofilms into biomineralized hybrid films composed of calcite and EPSs in a simulated marine medium, showing strong corrosion inhibition and self-healing activity. By comparing the wild-type strain of *P. lipolytica*, a strain overproducing EPSs and a strain lacking EPS production, it was confirmed that the EPS-overproducing strain had stronger corrosion inhibition, indicating that the formation of protective biomineralization films was closely related to EPSs.

¹Beijing Advanced Innovation Center for Materials Genome Engineering, Institute for Advanced Materials and Technology, University of Science and Technology Beijing, 100083 Beijing, China. ²National Materials Corrosion and Protection Data Center, University of Science and Technology Beijing, 100083 Beijing, China. ³BRI Southeast Asia Network for Corrosion and Protection (MOE), Shunde Graduate School of University of Science and Technology Beijing, 528399 Foshan, China. ⁴These authors contributed equally: Yuntian Lou, Weiwei Chang. ✉email: dzhang@ustb.edu.cn

In this study, the influence of biomineralization caused by *S. putrefaciens* on the MICI of Q235 carbon steel was investigated. The surface morphologies of Q235 carbon steel after immersion with and without *S. putrefaciens* were observed using scanning electron microscopy (SEM). The biofilm was evaluated using confocal laser scanning microscopy (CLSM). The MICI behaviors of the Q235 carbon steel were investigated based on measurements of weight loss, potentiodynamic polarization curves, and scanning electrochemical microscopy (SECM). The compositions of the surface product in media with and without *S. putrefaciens* were investigated using energy-dispersive spectrometry (EDS) and X-ray photoelectron spectroscopy (XPS). The compositions and microstructures of the mineralized particles were analyzed using X-ray diffraction (XRD) and transmission electron microscopy (TEM). Soluble iron and calcium were analyzed using inductively coupled plasma mass spectrometry (ICP-MS). The wear resistance of the mineralized layers was tracked by weight loss assays and surface morphology changes under mixed sand–water erosion conditions.

RESULTS AND DISCUSSION

Corrosion morphologies

Figure 1 shows the morphology of the surface products on the carbon steel coupon after immersion in sterile and *S. putrefaciens*-inoculated media for 7 and 14 days. In Fig. 1b and e, optical images of the macroscopic corrosion morphology on the 14th day are shown in the red frame. In Fig. 1b, a large number of reddish-brown corrosion products were uniformly deposited on the coupon surface. In contrast, grayish surface products instead of typical rust-like corrosion products were observed to uniformly cover the coupon surface in the *S. putrefaciens*-inoculated medium (Fig. 1e). The SEM images showed that a large quantity of corrosion products accumulated and formed a uniform layer on the coupon surface after immersion in the sterile medium for 14 days (Fig. 1b). In the enlarged image (Fig. 1c), it was observed that the corrosion product layer was extremely loose. The cracks observed on the surface of the corrosion product layer may result from the drying process³⁰. In the *S. putrefaciens*-inoculated medium, a large number of evenly distributed particles appeared on the coupon surface after 7 days of immersion (Fig. 1d). The number of particles further increased after 14 days, and the coupon surface was completely covered by a product layer composed of these particles (Fig. 1e). In the enlarged image (Fig. 1f), the particles were observed to have rhombohedral or trigonal structures, which were stacked on top of each other to form dense mineral-like layers.

Figure 2 shows the surface morphology of the Q235 coupons under different culture conditions after removing the surface product. The coupons in the *S. putrefaciens*-inoculated medium exhibited almost no corrosion after immersion for 7 days, and the abraded scratches on the coupon surface were visible. Even after 14 days of immersion, scratches on the coupon surface could still be observed, with only slight corrosion occurring on the local coupon surface. In contrast, serious uniform corrosion was observed on the coupons immersed in the sterile medium on the 7th and 14th days. These results indicated that the corrosion of the Q235 steel was significantly inhibited due to the presence of *S. putrefaciens*.

Biofilm observation

Figure 3 shows CLSM images of the biofilms formed on the surface of the Q235 carbon steel coupon after 7 and 14 days of immersion. A large number of bacteria uniformly adhered to the Q235 steel surface. After immersion for 7 days, the biofilm thickness was ~16 μm (Fig. 3a). In Fig. 3b, the biofilm thickness on the 14th day increased to ~22 μm . Notably, the blue areas represented mineralized particles between bacterial clusters on

the coupon surface (Fig. 3c, d). In the process of microbial-induced mineralization, the bacterial cell wall acts as a crystal nucleation site³¹. A mineralized envelope is then formed around the cell and impedes access to nutrients, which may explain the observation that a large number of dead bacteria were distributed in the biofilm on the 14th day.

In the cross-sectional images, the blue signal in Fig. 3d was more intense than that in Fig. 3c, indicating that the microbial-induced mineralization layers became thicker and more uniform after 14 days of immersion. The suspended living *S. putrefaciens* continuously adhered to the coupon surface to form mineral layers.

Analysis of the surface products

Figure 4a, b shows the SEM images of *S. putrefaciens* cells on the steel surface in the early stage of immersion. After 3 days of immersion, relatively loose flaky minerals appeared on the *S. putrefaciens* cell wall. As the immersion time increased, the flaky minerals became very dense, and they completely wrapped the *S. putrefaciens* cell on the 7th day. EDS analysis (Fig. 4c, d) showed a high level of calcium in the flaky minerals on the bacterial surface. These results combined with the analysis of carbon and oxygen content indicated that the flaky minerals may be calcium carbonate. Compared with that of point 1, the calcium content of point 2 increased slightly from 18.56 to 21.92%, while the iron content of point 2 decreased significantly from 18.74 to 5.43%. Based on these results, it was evident that the mineral layers on the coupon surface were induced by *S. putrefaciens*, and the degree of mineralization increased with time³².

X-ray diffraction (XRD) was used to further analyze the composition of the mineral layer (Supplementary Fig. 1). The mineral particles were mechanically removed from the product layer on the coupons using a steel scraper in *S. putrefaciens*-inoculated medium after 14 days. According to the XRD results, the mineral particles were mainly composed of calcite. The identified peaks of calcite at 2θ values of 23.25°, 29.48°, and 36.18° correlated with lattice indices of (012), (104) and (110), respectively^{33,34}. Figure 5 shows TEM and EDS images of a single-mineral particle³⁵. The mineral particle had a rhombohedral structure. The selected area electron diffraction (SAED) pattern in Fig. 5b shows clear diffraction spots and fuzzy diffuse rings, which indicated that the mineral particle was a mixture of polycrystalline and amorphous structures. The high-resolution TEM analyses in Fig. 5c showed that the mineral precipitates were polycrystalline with at least three planes. The lattice spacings of the precipitates were 0.19, 0.23, and 0.29 nm, corresponding to the (116), (113), and (006) planes, respectively (Fig. 5c). The elemental maps showed that the mineral particles were dominated by C, O, and Ca, which were distributed evenly. Consistent with the XRD analysis, the lattice-spacing pattern further confirmed that the precipitates were calcite, which is the most stable crystal structure of calcium carbonate.

To further investigate the influence of microbiologically induced mineralization on the corrosion behavior, the high-resolution Fe_{2p} , Ca_{2p} , C_{1s} , and O_{1s} peaks of the XPS spectra of the steel coupons incubated with and without *S. putrefaciens* for 14 days were compared (Fig. 6). The corresponding binding energy of each compound is listed in Table 1. The high-resolution Fe_{2p} spectra of the corrosion products of the Q235 steel in the sterile and *S. putrefaciens*-inoculated media are shown in Fig. 6a. The Fe_{2p} spectra can be fitted with three peaks, namely, FeOOH , Fe_2O_3 , and Fe_3O_4 ^{36,37}. Compared with the peak intensity in the spectrum of the steel immersed in the *S. putrefaciens*-inoculated medium, that in the spectrum of the steel immersed in the sterile medium was stronger, and the peak was attributed mainly to oxides and hydroxides of trivalent iron, indicating more serious corrosion. Figure 6b presents the high-resolution Ca_{2p} spectra, and the peaks at 351.1 and 347.1 eV were assigned to calcium carbonate.

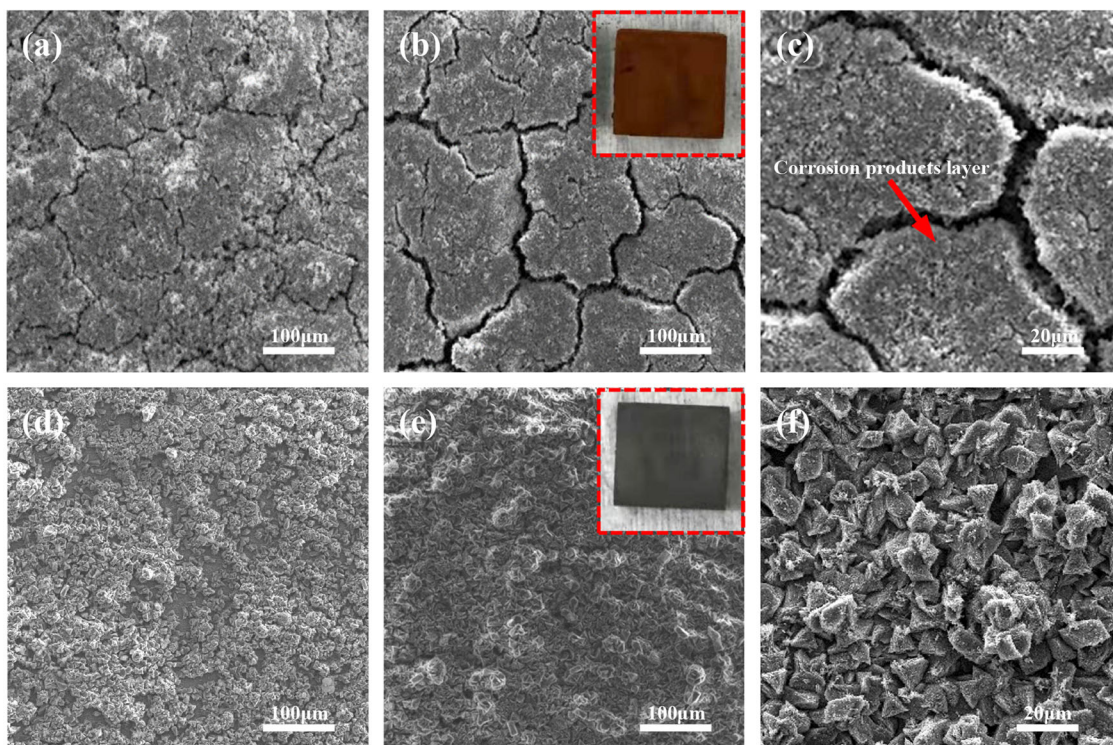


Fig. 1 SEM and optical images of the surface products on the Q235 coupons. **a, b** Q235 surface in the sterile medium after 7 days and 14 days; **d, e** Q235 surface in *S. putrefaciens*-inoculated medium after 7 days and 14 days. **c** Enlarged image of panel **b**. **f** Enlarged image of panel **e**.

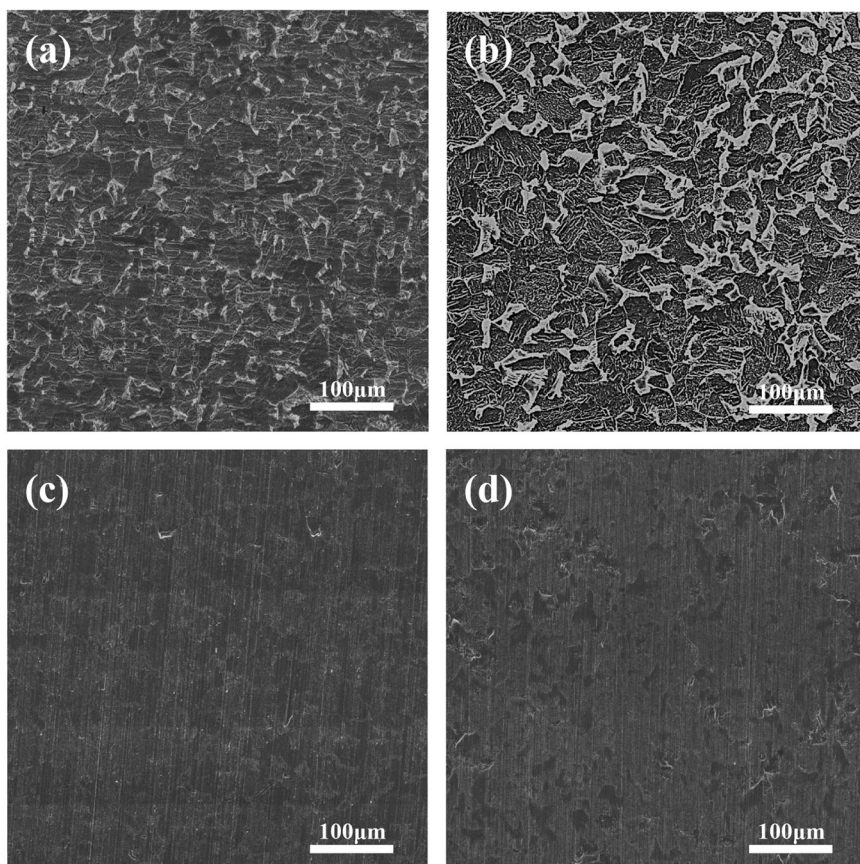


Fig. 2 SEM images of Q235 coupons after removing the surface products. **a, b** Q235 surface in the sterile medium after 7 days and 14 days; **c, d** Q235 surface in *S. putrefaciens*-inoculated medium after 7 days and 14 days.

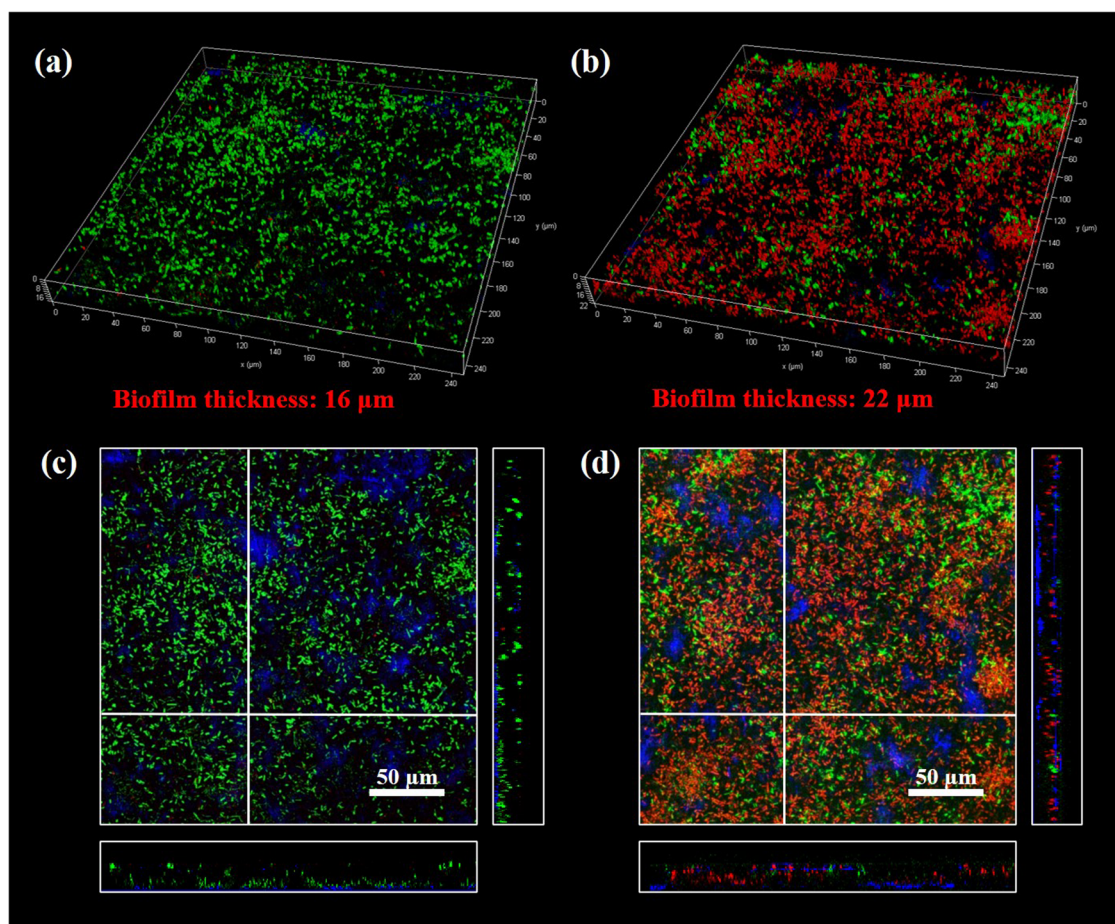


Fig. 3 CLSM images of *S. putrefaciens* biofilms on the surfaces of the Q235 carbon steel coupon. **a, c** after 7 days and **b, d** after 14 days.

The intensity of the Ca_{2p} peak for the coupon immersed in the *S. putrefaciens*-inoculated medium was much stronger than that for the sample immersed in the sterile medium. These results indicated that the presence of *S. putrefaciens* could form mineral layers with calcium carbonate as the main component on the steel surface and could effectively inhibit corrosion. Figure 6c, d presents the high-resolution C_{1s} and O_{1s} spectra. The C_{1s} spectrum could be fitted with three peaks, corresponding to C-(C, H), C-(O, N), and CO_3^{2-} ^{38,39}. The CO_3^{2-} signal peak in the *S. putrefaciens*-inoculated medium was mainly attributed to calcium carbonate mineral layers. In the sterile medium, the CO_3^{2-} signal peak may be attributed to the adsorption of CO_3^{2-} on the loose rust layer from the 2216E medium. Similarly, the stronger C-(C, H) signal in the sterile medium may also be attributed to the adsorption of organics from the 2216E medium. The O_{1s} spectrum could be fitted with five peaks, namely, O^{2-} , OH, carbonate, organic O, and H_2O . The O^{2-} peak was attributed to iron oxides in the rust layers. Its strength was obviously lower in the spectrum for the sample in the *S. putrefaciens*-inoculated medium, which was consistent with the results of the Fe high-resolution spectrum. Notably, the peaks of organic O and H_2O were detected in the spectrum of the sample immersed in the *S. putrefaciens*-inoculated medium. The peak of organic O was attributed to the EPSs mixed in the mineral layer, and the H_2O peak may be attributed to calcium carbonate monohydrate, which is the thermodynamic metastable phase of calcium carbonate^{40,41}.

ICP-MS

Supplementary Fig. 2 shows the concentrations of calcium ions and iron ions released from the steel coupons immersed in the

sterile medium and the *S. putrefaciens*-inoculated medium for 3, 7, 11, and 14 days. The concentration of calcium ions in the sterile medium did not change substantially. However, the concentration of calcium ions in the *S. putrefaciens*-inoculated medium gradually decreased with the increase in immersion time. In the mineralization process, bacteria were used as carriers for the nucleation and growth of minerals, and their metabolites provided an environment of high local alkalinity and supersaturation of carbonate for mineral formation⁴². Combined with the results in Supplementary Fig. 3 indicate that the cell concentration and pH value of *S. putrefaciens* in the stationary phase were maintained at a high level after 7 days. In Supplementary Fig. 2a, the concentration of calcium ions in the *S. putrefaciens*-inoculated medium was approximately half the initial concentration on the 11th day, indicating that calcium deposition was closely related to the metabolic intensity of *S. putrefaciens*.

Supplementary Fig. 2b, the iron ion concentrations in the sterile medium substantially increased as the immersion time increased as a result of the corrosion of the steel surface. In contrast, the iron concentration was almost unchanged in the *S. putrefaciens*-inoculated medium. This indicated that *S. putrefaciens* effectively inhibited the dissolution of the steel, with only a small quantity of iron ions released at the beginning of immersion. When the bacterial growth reached the stationary phase, corrosion was inhibited with the maturation of the mineral layers.

Potentiodynamic polarization and weight loss measurements

Figure 7a shows the potentiodynamic polarization curves of the Q235 steel in the sterile and *S. putrefaciens*-inoculated media after

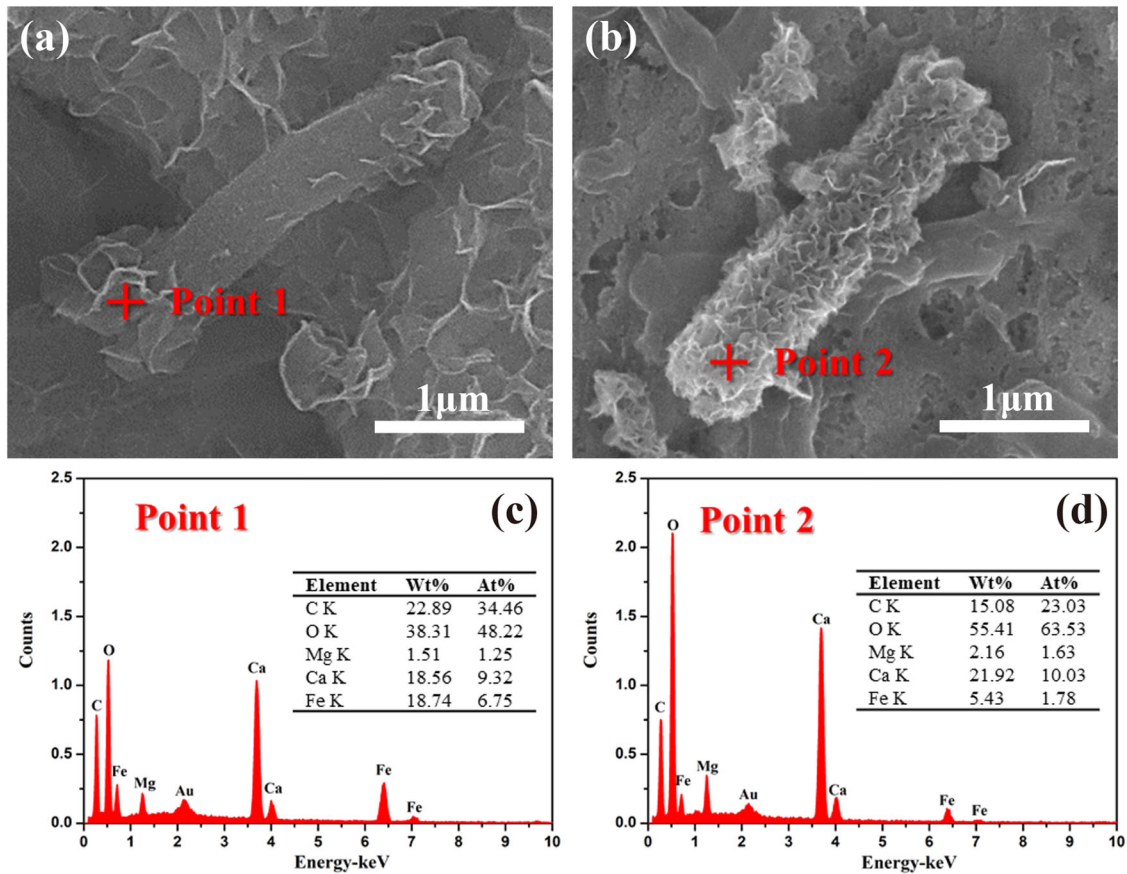


Fig. 4 SEM and EDS images of *S. putrefaciens* cells on the surface of a Q235 coupon. **a** Third day, **b** seventh day, **c** point 1, **d** point 2.

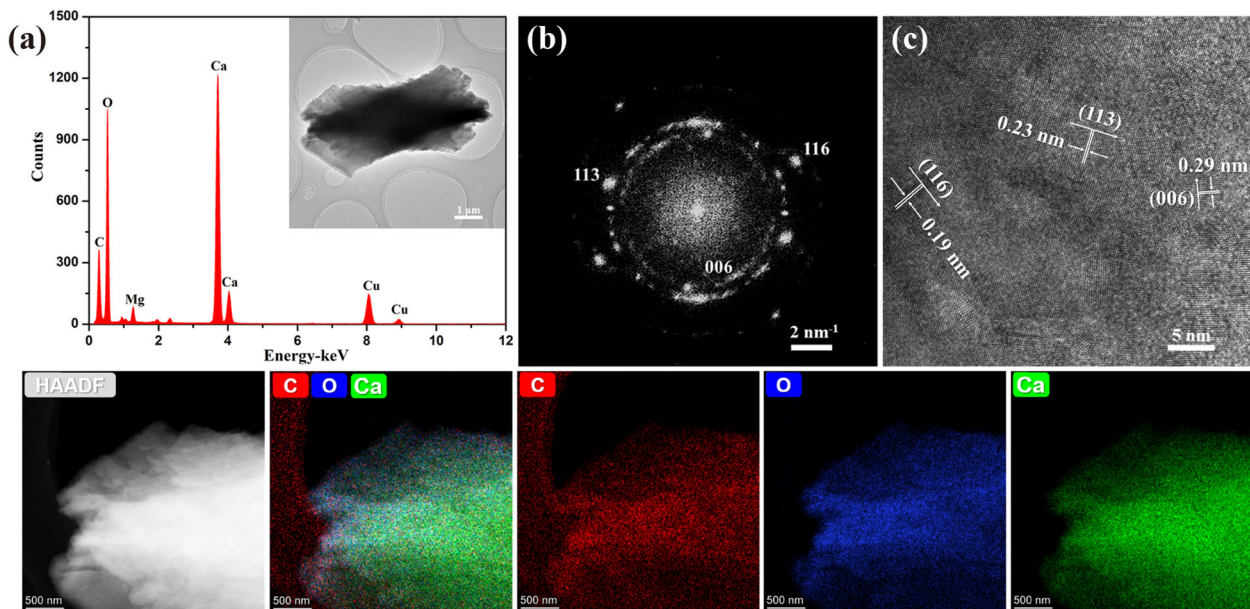


Fig. 5 TEM and EDS images of precipitates on the Q235 coupon after 14 days. **a** TEM and EDS images of a mineral particle from the Q235 coupon surface; **b** SAED pattern; **c** high-resolution transmission electron microscopy (HRTEM) analyses. The elemental maps show that C, O, and Ca were evenly distributed on the particle surface.

14 days of immersion. Compared with the steel immersed in the sterile medium, the sample in the *S. putrefaciens*-inoculated medium showed a significantly reduced corrosion current density ($0.38 \mu\text{A cm}^{-2}$), which was less than one-tenth that in the sterile

medium ($4.86 \mu\text{A cm}^{-2}$). To further investigate the effect of *S. putrefaciens* on corrosion inhibition, the corrosion rates of the steel were determined by weight loss measurements after 3, 7, 11, and 14 days of immersion. According to Fig. 7b, the corrosion rate

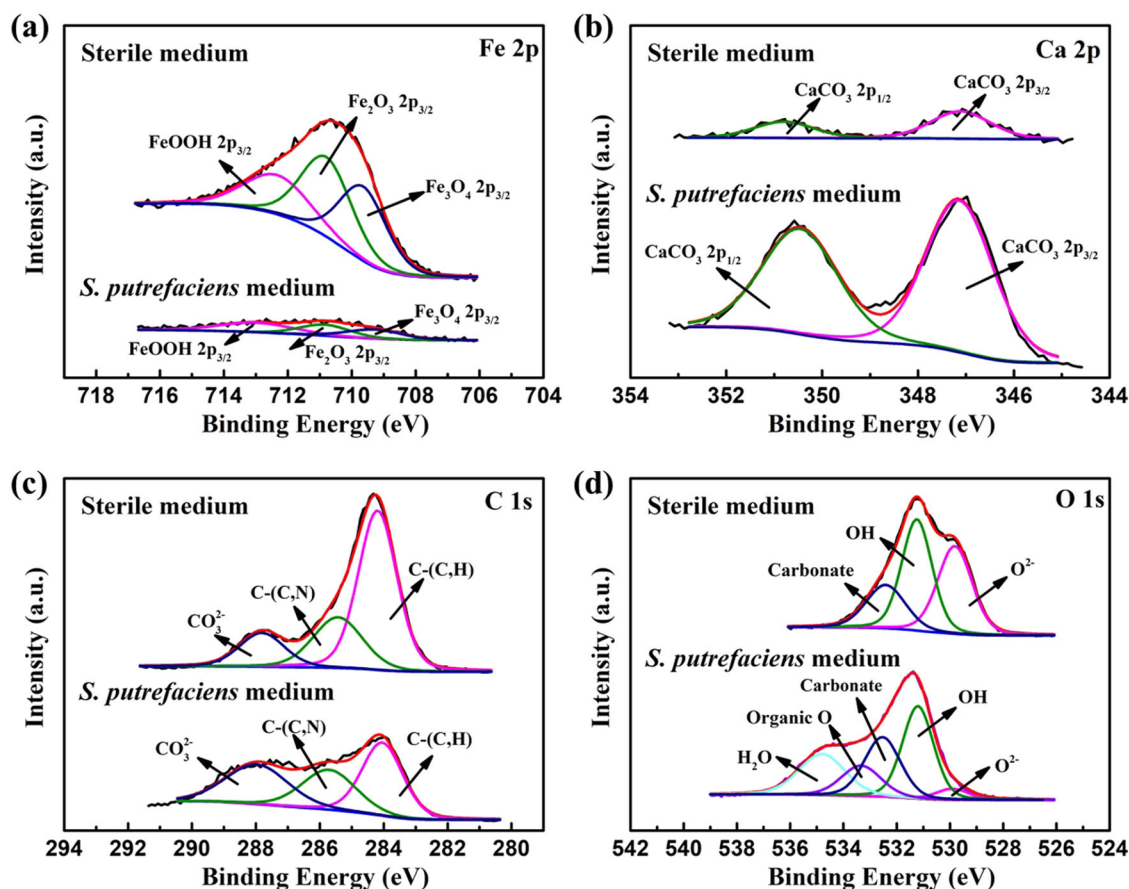


Fig. 6 High-resolution XPS spectra for the Q235 surface after immersion in sterile medium and in *S. putrefaciens*-inoculated medium for 14 days. **a–d** correspond to Fe_{2p} , Ca_{2p} , C_{1s} , and O_{1s} , respectively.

Table 1. Binding energies of elements on the Q235 coupon surface from XPS.					
Elements	Peak	Binding energy (eV)	Elements	Peak	Binding energy (eV)
Fe 2p	Fe_2O_3	710.40 ± 0.1	Ca 2p	Ca 2p _{1/2}	351.1 ± 0.1
	Fe_3O_4	708.20 ± 0.1		Ca 2p _{3/2}	347.1 ± 0.1
	FeOOH	711.80 ± 0.1	O 1s	O^{2-}	530.1 ± 0.1
C 1s	C-(C, H)	284.2 ± 0.1	OH	531.8 ± 0.2	
	C-(O, N)	285.9 ± 0.1	Carbonate	532.3 ± 0.2	
	CO_3^{2-}	288.4 ± 0.1	Organic O	533.3 ± 0.1	
			H_2O	534.8 ± 0.1	

in the *S. putrefaciens*-inoculated medium was much lower than that in the sterile medium at every time point. After 14 days, the corrosion rate in the *S. putrefaciens*-inoculated medium (0.004 mm y^{-1}) was also less than one-tenth that in the sterile medium (0.052 mm y^{-1}), which was consistent with the results of the potentiodynamic polarization measurements.

To further elucidate the contribution of mineralized layers to corrosion inhibition, weight loss measurements were conducted in a calcium-free bacterial culture medium. The results showed that the corrosion was inhibited especially in the early stage (3 and 7 days) due to the presence of *S. putrefaciens*. However, the corrosion rates began to rise remarkably with extended immersion (11 and 14 days). In the early stage of the test, the *S. putrefaciens* biofilm had strong metabolic activity and can consume a large amount of dissolved

oxygen, thereby suppressing the cathodic corrosion reactions. However, as the bacteria cells died after a longer culture time and the bacterial aerobic respiration intensity weakened, the corrosion rate began to increase. These results suggest that both the mineral formation and the biofilm can contribute to the mitigation of corrosion. The formation of a mineralized layer could provide longer-acting corrosion protection of the steel substrate.

Wear resistance

Wear resistance is an important property for a protective layer, especially in marine environments, where sandy seawater can easily cause erosion. The weight loss during the wear test was tracked to evaluate the wear resistance of *S. putrefaciens*-induced mineral layers. Figure 8a shows a schematic illustration of the wear-resistance testing equipment. The coupon was firmly adhered to the turntable and completely immersed in artificial seawater containing silica sand. The coupon was rotated at a speed of 1 m s^{-1} for 30-min cycles and weighed at the end of each cycle. In Fig. 8b, the weight loss was relatively fast in the first six cycles, which may be due to the weak adhesion of the mineral particles in the upper layer of the mineral layers. In the last four cycles, the erosion of the mineralized layer slowed significantly, indicating that the bottom of the mineralized layers was more cohesive and exhibited better protection performance. Supplementary Fig. 4 shows the SEM images of the Q235 coupon surface before and after the wear-resistance test. In Supplementary Fig. 4b, the surface morphology of the mineralized layer after ten cycles in the wear-resistance test was almost the same as the original morphology. The mineral particles still maintained sharp edges (Supplementary Fig. 4d). This result is consistent with

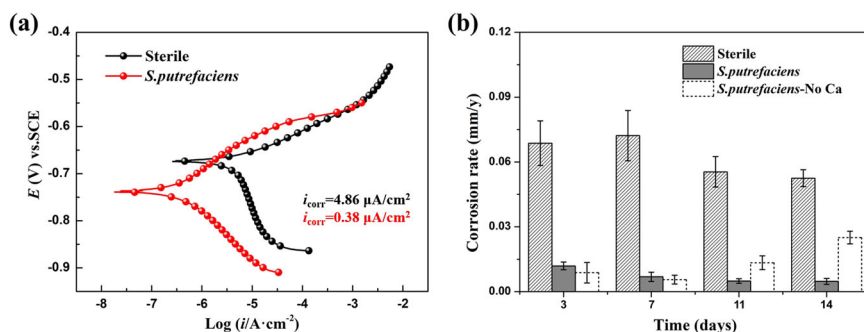


Fig. 7 Evaluation of microbiologically influenced corrosion inhibition. **a** Potentiodynamic polarization curves; **b** corrosion rates of Q235 coupons in the sterile medium, in the *S. putrefaciens*-inoculated medium, and in the *S. putrefaciens*-inoculated medium without calcium.

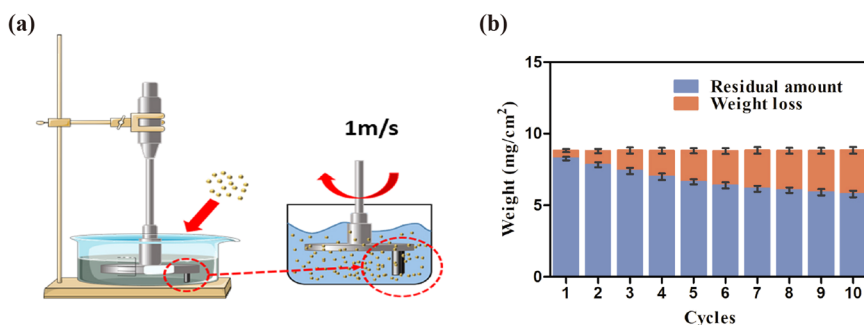


Fig. 8 Wear resistance of *S. putrefaciens*-induced mineral layers. **a** Schematic illustration of wear-resistance testing equipment; **b** weight loss of the coupons after different testing cycles.

the weight loss data, indicating that the mineralized layer has wear resistance⁴³.

In situ microbial self-healing effect of mineral layers

In actual marine environments, damage to material surfaces by mechanical and chemical attacks is inevitable. Microbial self-healing can repair the damage sustained by the protective layer and restore the physical shielding performance. Figure 9a shows the CLSM images of the surface of the mineral layers formed by *S. putrefaciens*, on which an artificial scratch with a width and depth of $\sim 40 \mu\text{m}$ was made. After 7 days of immersion in the *S. putrefaciens*-inoculated medium, the deposition of mineral particles induced a self-healing effect of the surface morphology. The scratch region was flattened, the width of the scratch was reduced from 39.71 to 31.27 μm , and the depth of the scratch was significantly reduced from 37.84 to 13.27 μm . After 14 days, the coupon surface was almost completely repaired, with only minor traces observed at the scratch region, with a depth of only 8.34 μm (Fig. 9f).

The in situ microbial self-healing effect on the corrosion protection property of the mineralized layer was investigated by SECM, which monitored the concentration of oxygen over the scratch region. Competition between oxygen reduction at the tip of the UME and the cathodic corrosion reaction on the Q235 steel surface caused the current reduction in the SECM image⁴⁴. In Fig. 9g, the current over the scratch region was sharply reduced, indicating that the oxygen in this area was almost completely consumed by the cathodic corrosion reaction on the exposed substrate. After 7 days, the scratch was covered with mineralized layers, which inhibited the progress of the cathodic reaction. In this case, the efficiency of the microbial self-healing effect, as determined by the I/I_a value at the scratch after microbial self-healing, was as high as 82%. As microbial self-healing continued, the crack was completely repaired on the 14th day.

The above results indicated that *S. putrefaciens*-induced mineralization plays a key role in MICI, and the mechanism of MICI is shown in Fig. 10. In the initial stage of immersion, *S. putrefaciens* in the logarithmic phase rapidly proliferates and secretes EPSs, which attach to the coupon surface to form biofilms. EPSs include a variety of organic macromolecules, such as proteins, polysaccharides and other substances, which can act as a physical barrier to hinder the diffusion of dissolved oxygen to the metal surface⁴⁵, and the functional groups, such as $-\text{COOH}$, $-\text{OH}$, and $-\text{NH}_2$, can be deprotonated with increasing pH, making the EPSs negatively charged overall⁴⁶. These features are beneficial for the chelation of calcium ions in solution and provide a favorable local environment for biomineralization⁴⁷. Under alkaline conditions, the carbon dioxide produced by aerobic respiration dissolves in water to generate HCO_3^- . *S. putrefaciens* uses the cell wall as the nucleation site to induce carbonate deposition to form mineralized layers. Under the condition of complete immersion, the biomineralization process impedes the diffusion of dissolved oxygen to the metal surface, and the cathode process is inhibited⁴⁸. Based on the above mechanism, the microorganisms only rely on the natural environment and their own metabolism to enable corrosion inhibition without the usage/release of toxic compounds and the additional manual intervention such as those associated with conventional corrosion mitigation methods. Thus, MICI based on bacterial mineralization is environmentally friendly and conforms to the direction of the development of anticorrosion technologies, although extensive laboratory and field studies are still needed to assess its viability in real and complex environmental conditions.

In summary, the influence of *S. putrefaciens* on the MICI behavior of Q235 carbon steel was investigated in this study. In contrast to the severe corrosion of carbon steel coupons in a sterile medium, corrosion of the coupons in an *S. putrefaciens*-inoculated medium was inhibited by the biomineralized layers induced by *S. putrefaciens*. The biomineralized layers were

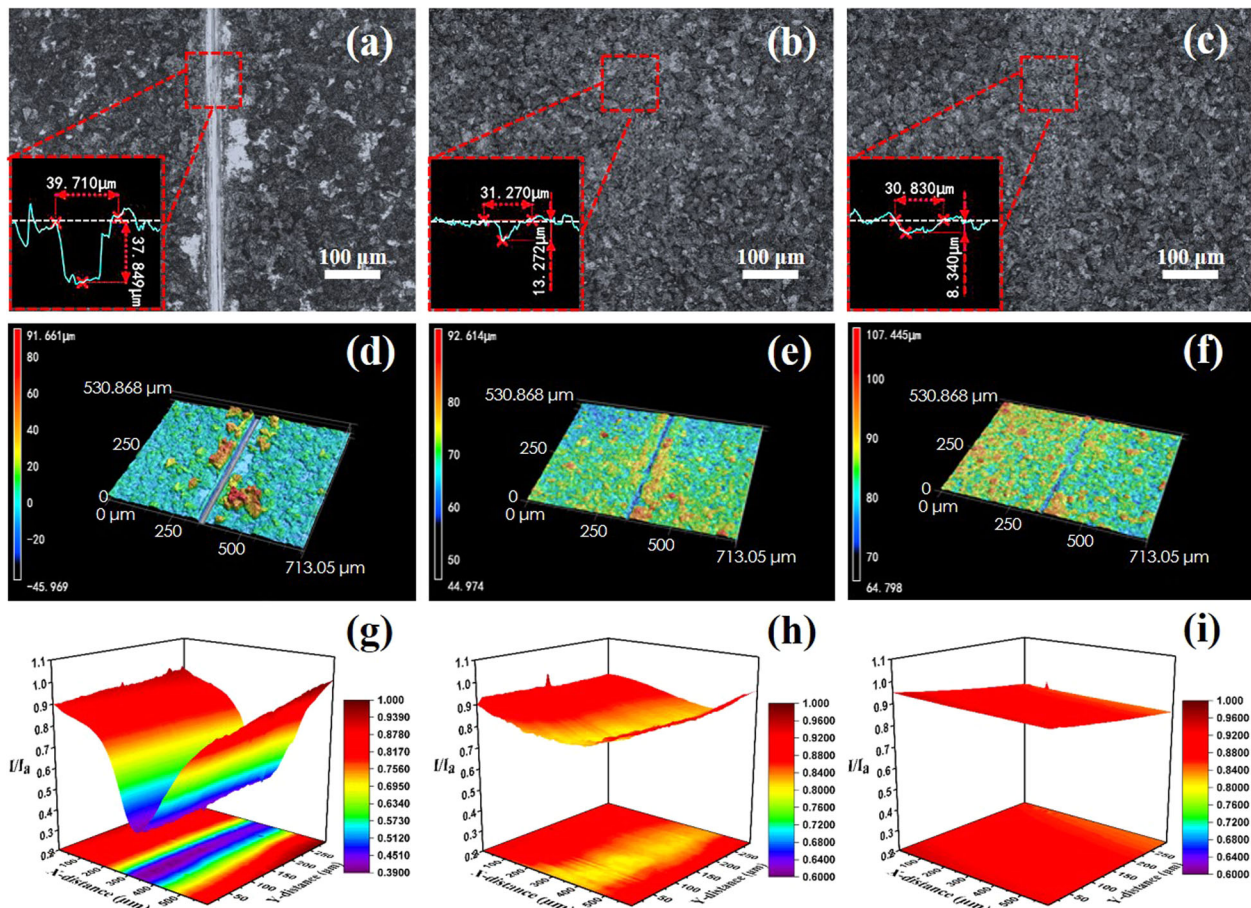


Fig. 9 Stereo-optical micrographs and SECM images of a coating scratch during the *S. putrefaciens*-induced microbial self-healing process. **a, d, g** Before microbial self-healing; **b, e, h** immersion for 7 days in the *S. putrefaciens*-inoculated medium; **c, f, i** immersion for 14 days in the *S. putrefaciens*-inoculated medium.

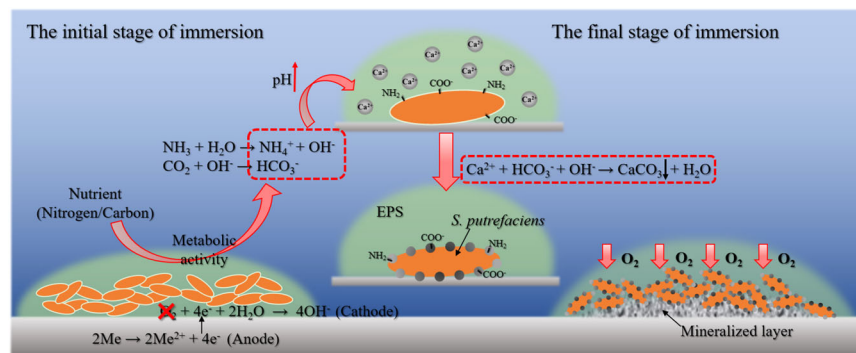


Fig. 10 Schematic illustration of the MICI mechanism via biomineralization induced by *S. putrefaciens*.

characterized in terms of morphology, composition, electrochemical behaviors, microbial self-healing performance and wear resistance. The following conclusions can be drawn:

1. According to the morphology observations, electrochemical tests, and weight loss assays, the formation of biomineralized layers induced by *S. putrefaciens* mitigated uniform corrosion on the carbon steel during 14 days of immersion.
2. The XRD, TEM, and XPS results demonstrated that the mineralized layer was a mixture of calcite and a small quantity of EPSs.
3. The results of wear resistance and SECM measurements indicated that the biomineralized layers induced by

S. putrefaciens possessed anti-abrasive and microbial self-healing properties, and the repaired surface had the same corrosion resistance as the complete mineralized layers.

METHODS

Bacteria and media

The pure *S. putrefaciens* strain was obtained from the Marine Culture Collection of China (MCCC). The *S. putrefaciens* strain was cultured in 2216E medium containing 5.0 g peptone, 1.0 g yeast extract, 0.1 g ferric citrate, 19.45 g NaCl, 5.98 g MgCl₂, 3.24 g Na₂SO₄, 1.8 g CaCl₂, 0.55 g KCl, 0.16 g Na₂CO₃, 0.08 g KBr, 0.034 g SrCl₂, 0.08 g SrBr₂, 0.022 g H₃BO₃, 0.004 g NaSiO₃, 0.0024 g NaF, 0.0016 g NH₄NO₃, and 0.008 g NaH₂PO₄ in 1 L deionized water. The pH of the

Table 2. Chemical composition of Q235 carbon steel (wt%).

Elements	C	Mn	Si	S	P	Fe
Content (wt%)	0.21	0.31	0.18	0.03	0.03	Balance

medium was 7.2 ± 0.2 . The 2216E medium was sterilized at 121°C for 20 min in an autoclave (Panasonic, MLS-3781-PC). The cell numbers of the planktonic *S. putrefaciens* were measured using a hemocytometer under a light microscope (Zeiss, Lab A1) at $\times 400$ magnification.

Materials and treatment

Q235 carbon steel coupons with dimensions of $10 \times 10 \times 3 \text{ mm}^3$ were used for all tests. Table 2 shows the chemical compositions (wt%) of Q235 carbon steel. All coupons were abraded sequentially with 200, 400, 600, and 800 grit sandpapers and then rinsed with ethanol, as described in the literature⁴⁹. Before each experiment, all the coupons were dried under ultraviolet light for 30 minutes. Immersion testing was conducted in a conical flask containing 50 ml liquid medium⁵⁰. Three identical coupons were placed at the bottom of each conical flask. The coupons were completely immersed in liquid medium and did not touch each other.

Surface characterization

Before and after removing the surface products, the morphologies were observed using SEM (Hitachi, SU8010). The surface products and the biofilm were removed by means of Clarke's solution according to ASTM G1-03⁵¹. Before observing the bacteria attached to the coupons, the coupons were fixed in 2.5% (v/v) glutaraldehyde at 4°C overnight and dehydrated with an ethanol gradient (50, 70, 85, 95, and 100 vol.%) to maintain the original morphology of the bacteria. The coupons were sputter-coated with Au to improve the surface conductivity before SEM observations. The biofilm on the coupon surface was observed using CLSM (Leica, TCS SP8) after live/dead fluorescent staining. The live and dead cells appeared green and red, respectively, as a result of SYTO-9 and propidium iodide (PI) dyes (Thermo Fisher, LIVE/DEAD™ BacLight™ Bacterial Viability Kit)⁵². The chemical compositions of the surface product layers were analyzed using X-ray diffraction (XRD, D8 Advance, Bruker) and XPS (Thermo Fisher, ESCALAB 250Xi). To evaluate the self-healing performance of *S. putrefaciens*, CLSM (Kenyence, VK-X260K) was used to observe the morphology of artificial defects before and after microbial self-healing.

Electrochemical measurements

Electrochemical measurements were performed using an electrochemical station (Gamry, Reference 600 Plus). The electrochemical behaviors of the Q235 carbon steel were evaluated using a traditional three-electrode system consisting of a Q235 coupon as the working electrode, platinum foil as the counter electrode, and a saturated calomel electrode (SCE) as the reference electrode. Before each electrochemical test, the open circuit potential (OCP) was measured for no less than 10 min to ensure measurement stability. Potentiodynamic polarization curves were obtained after 14 days of immersion in sterile and *S. putrefaciens*-inoculated media, and the scanning potential range was from $-200 \text{ mV}_{\text{SCE}}$ to $+200 \text{ mV}_{\text{SCE}}$ vs. OCP at a scanning rate of 0.166 mV s^{-1} .

SECM measurements were performed using a microelectrochemical station (CH Instruments, 920D). The measurements were conducted by means of a four-electrode system consisting of the traditional three-electrode system and a platinum ultramicroelectrode (UME) as another working electrode⁵³. The UME was composed of a platinum wire with a diameter of $10 \mu\text{m}$ encapsulated in a borosilicate glass capillary. According to the approach curve, the distance between the UME probe tip and the coupon surface was maintained at $25 \mu\text{m}$. The probe was scanned on the XY plane over an area of $300 \times 500 \mu\text{m}^2$ at a scanning rate of $50 \mu\text{m s}^{-1}$. In redox competitive mode, a constant potential of -0.6 V (Ag/AgCl) was applied to the probe tip to collect oxygen reduction signals. The oxygen reduction current (I) obtained in the artificial crack region was normalized to the current (I_a) obtained over the intact region⁵⁴. The I/I_a values were used to evaluate the healing efficiency.

Weight loss assay and ICP-MS

Before the immersion tests, all coupons were weighed and recorded using an electronic balance (ME204, Mettler Toledo). After immersing the coupons for different times and removing the surface products according to ISO 8407, the coupons were rinsed with deionized water, dried with nitrogen and weighed again⁵⁵. The uniform corrosion rate (mm y^{-1}) was calculated from the weight loss data using the following equation:

$$V_{\text{corr}} = \frac{8.76 \times 10^4 \times \Delta m}{\rho A t} \quad (1)$$

where V_{corr} is the corrosion rate (mm y^{-1}); ρ is the coupon density (g cm^{-3}); A is the exposed coupon area (cm^2); t is the testing time (h); and Δm is the difference between the weights of the coupon before and after immersion.

The concentrations of calcium and iron ions in the medium were evaluated using ICP-MS (Thermo Scientific, iCAP TQs). Sterile and *S. putrefaciens*-inoculated media with different immersion times were pretreated with concentrated nitric acid and then tested.

Wear-resistance test

The wear resistance of the mineral layers on the Q235 carbon steel coupons was evaluated using abrasive erosion testing equipment⁵⁶. A sand–water mixture with a mass ratio of 1:20 was added to the water tank. The coupons were firmly glued to the edge of the rotating disk of the equipment, and the coupon working surface was perpendicular to the ground. During the test, the disk was rotated at a constant linear velocity of 1 m s^{-1} in 30-min cycles. After completing each cycle, the coupons were removed from the equipment, washed with deionized water, dried with nitrogen, and weighed. The wear resistance of the mineral layers was evaluated in terms of weight loss. Before the wear-resistance test, the original weight of the coupons with mineral layers was determined by means of an electronic analytical balance with a precision of 0.1 mg. After each cycle, the coupons were washed with deionized water and ethanol, dried with nitrogen, and weighed.

DATA AVAILABILITY

The data of this study are available from the corresponding authors upon reasonable requests.

Received: 16 June 2021; Accepted: 18 October 2021;

Published online: 30 November 2021

REFERENCES

- Li, X. G. et al. Materials science: share corrosion data. *Nature* **527**, 441–442 (2015).
- Hou, B. et al. The cost of corrosion in China. *Npj Mater. Degrad.* **1**, 1–10 (2017).
- Zhang, F. et al. Self-healing mechanisms in smart protective coatings: a review. *Corros. Sci.* **144**, 74–88 (2018).
- Cai, H., Wang, P., Zhang, D., Wang, Y. & Li, E. An intelligent self-defensive coating based on sulfide ion responsive nanocontainers for suppression of micro-biologically influenced corrosion induced by sulfate reducing bacteria. *Corros. Sci.* **188**, 109543 (2021).
- Wang, P., Li, T. & Zhang, D. Fabrication of non-wetting surfaces on zinc surface as corrosion barrier. *Corros. Sci.* **128**, 110–119 (2017).
- Dou, W., Wu, J., Gu, T., Wang, P. & Zhang, D. Preparation of super-hydrophobic micro-needle CuO surface as a barrier against marine atmospheric corrosion. *Corros. Sci.* **131**, 156–163 (2018).
- Rémazeilles, C., Lévêque, F., Conforto, E. & Refait, P. Long-term alteration processes of iron fasteners extracted from archaeological shipwrecks aged in biologically active waterlogged media. *Corros. Sci.* **181**, 109231 (2021).
- Kip, N. & van Veen, J. A. The dual role of microbes in corrosion. *ISME J.* **9**, 542–551 (2015).
- Videla, H. A. & Herrera, L. K. Understanding microbial inhibition of corrosion. A comprehensive overview. *Int. Biodeterior. Biodegrad.* **63**, 896–900 (2009).
- Little, B., Lee, J. & Ray, R. A review of 'green' strategies to prevent or mitigate micro-biologically influenced corrosion. *Biofouling* **23**, 87–97 (2007).
- Little, B. & Ray, R. A perspective on corrosion inhibition by biofilms. *Corrosion* **58**, 424–428 (2002).
- Lou, Y. et al. Microbiologically influenced corrosion inhibition mechanisms in corrosion protection: a review. *Bioelectrochemistry* **141**, 107883 (2021).

13. AlAbbas, F. M., Bhola, S. M., Spear, J. R., Olson, D. L. & Mishra, B. The shielding effect of wild type iron reducing bacterial flora on the corrosion of linepipe steel. *Eng. Fail Anal.* **33**, 222–235 (2013).
14. Kip, N. et al. Methanogens predominate in natural corrosion protective layers on metal sheet piles. *Sci. Rep.* **7**, 11899 (2017).
15. In, T. et al. High-level abundances of Methanobacteriales and Syntrophobacteriales may help to prevent corrosion of metal sheet piles. *Appl. Environ. Microbiol.* **85**, 01369–01319 (2019).
16. Jonkers, H. M., Thijssen, A., Muyzer, G., Copuroglu, O. & Schlangen, E. Application of bacteria as self-healing agent for the development of sustainable concrete. *Ecol. Eng.* **36**, 230–235 (2010).
17. Wiktor, V. & Jonkers, H. M. Quantification of crack-healing in novel bacteria-based self-healing concrete. *Cem. Concr. Compos.* **33**, 763–770 (2011).
18. Xu, J., Tang, Y. & Wang, X. A correlation study on optimum conditions of microbial precipitation and prerequisites for self-healing concrete. *Process. Biochem.* **94**, 266–272 (2020).
19. Minto, J. M. et al. 'Microbial mortar'-restoration of degraded marble structures with microbially induced carbonate precipitation. *Constr. Build Mater.* **180**, 44–54 (2018).
20. Qian, C., Zheng, T., Zhang, X. & Su, Y. Application of microbial self-healing concrete: case study. *Constr. Build Mater.* **290**, 123226 (2021).
21. Liu, L., Ji, J., Guo, Y. & Chen, J. Use of ecological concrete for nutrient removal in coastal sediment and its effects on sediment microbial communities. *Mar. Pollut. Bull.* **162**, 111911 (2021).
22. Krajewska, B. Urease-aided calcium carbonate mineralization for engineering applications: a review. *J. Adv. Res.* **13**, 59–67 (2018).
23. Zhu, T. & Ditttrich, M. Carbonate precipitation through microbial activities in natural environment, and their potential in biotechnology: a review. *Front Bioeng. Biotechnol.* **4**, 4–4 (2016).
24. Qin, W. et al. Microbe-mediated extracellular and intracellular mineralization: environmental, industrial, and biotechnological applications. *Adv. Mater.* **32**, e1907833 (2020).
25. Liu, S. et al. Effectiveness of the anti-erosion of a MICP coating on the surfaces of ancient clay roof tiles. *Constr. Build Mater.* **243**, 118202 (2020).
26. Ortega-Villamagua, E., Gudino-Gomezjurado, M. & Palma-Cando, A. Microbiologically induced carbonate precipitation in the restoration and conservation of cultural heritage materials. *Molecules* **25**, 5499 (2020).
27. Tang, C. et al. Factors affecting the performance of microbial-induced carbonate precipitation (MICP) treated soil: a review. *Environ. Earth Sci.* **79**, 94 (2020).
28. Xu, J., Tang, Y., Wang, X., Wang, Z. & Yao, W. Application of ureolysis-based microbial CaCO₃ precipitation in self-healing of concrete and inhibition of reinforcement corrosion. *Constr. Build Mater.* **265**, 120364 (2020).
29. Liu, T. et al. Marine bacteria provide lasting anticorrosion activity for steel via biofilm-induced mineralization. *ACS Appl. Mater. Interfaces* **10**, 40317–40327 (2018).
30. Wang, Y. et al. Corrosion of EH40 steel affected by *Halomonas titanicae* dependent on electron acceptors utilized. *Corros. Sci.* **182**, 109263 (2021).
31. De Muynck, W., De Belie, N. & Verstraete, W. Microbial carbonate precipitation in construction materials: a review. *Ecol. Eng.* **36**, 118–136 (2010).
32. Sazanova, K. V. et al. Carbonate and oxalate crystallization by interaction of calcite marble with *Bacillus subtilis* and *Bacillus subtilis*-*Aspergillus niger* association. *Crystals* **10**, 756 (2020).
33. Ghosh, T., Bhaduri, S., Montemagno, C. & Kumar, A. *Sporosarcina pasteurii* can form nanoscale calcium carbonate crystals on cell surface. *PLoS ONE* **14**, e0210339 (2019).
34. Helmi, F. M., Elmitwalli, H. R., Elnagdy, S. M. & El-hagrassy, A. F. Biomineralization consolidation of Fresco wall paintings samples by *Bacillus sphaericus*. *Geomicrobiol. J.* **33**, 625–629 (2016).
35. Enyedi, N. T. et al. Cave bacteria-induced amorphous calcium carbonate formation. *Sci. Rep.* **10**, 8696 (2020).
36. Li, Y. et al. Bacterial distribution in SRB biofilm affects MIC pitting of carbon steel studied using FIB-SEM. *Corros. Sci.* **167**, 108512 (2020).
37. Li, Z. et al. Corrosion behavior of X80 pipeline steel in the presence of *Brevibacterium halotolerans* in Beijing soil. *Bioelectrochemistry* **126**, 121–129 (2019).
38. Jin, J., Wu, G., Zhang, Z. & Guan, Y. Effect of extracellular polymeric substances on corrosion of cast iron in the reclaimed wastewater. *Bioresour. Technol.* **165**, 162–165 (2014).
39. Liu, H., Gu, T., Zhang, G., Liu, H. & Cheng, Y. F. Corrosion of X80 pipeline steel under sulfate-reducing bacterium biofilms in simulated CO₂-saturated oilfield produced water with carbon source starvation. *Corros. Sci.* **136**, 47–59 (2018).
40. Gubner, R. & Beech, I. The effect of extracellular polymeric substances on the attachment of *Pseudomonas NCIMB 2021* to AISI 304 and 316 stainless steel. *Biofouling* **15**, 25–36 (2000).
41. Salvi, A. M., Langerame, F., Pace, A. E., Carbone, M. E. E. & Ciriello, R. Comparative spectra illustrating degradation of Ca₂O₄·H₂O during XPS analysis. *Surf. Sci. Spectra* **22**, 21–31 (2015).
42. Andritsos, N., Kontopoulou, M., Karabelas, A. & Koutsoukos, P. Calcium carbonate deposit formation under isothermal conditions. *Can. J. Chem. Eng.* **74**, 911–919 (1996).
43. Oladele, I. O., Akinwekomi, A. D., Agbabiaka, O. G. & Oladejo, M. O. Influence of biodegradation on the tensile and wear resistance properties of bio-derived CaCO₃/epoxy composites. *J. Polym. Res.* **26**, 1–9 (2019).
44. González-García, Y., García, S. J., Hughes, A. E. & Mol, J. M. C. A combined redox-competition and negative-feedback SECM study of self-healing anticorrosive coatings. *Electrochem Commun.* **13**, 1094–1097 (2011).
45. Kuklinski, A. & Sand, W. in *Encyclopedia of Applied Electrochemistry* (Springer New York, 2014).
46. Castro-Alonso, M. J. et al. Microbially induced calcium carbonate precipitation (MICP) and its potential in bioconcrete: microbiological and molecular concepts. *Front. Mater.* **6**, 126 (2019).
47. Dupraz, C. et al. Processes of carbonate precipitation in modern microbial mats. *Earth Sci. Rev.* **96**, 141–162 (2009).
48. Liu, Z. et al. Study of corrosion behavior of carbon steel under seawater film using the wire beam electrode method. *Corros. Sci.* **80**, 523–527 (2014).
49. Lou, Y. et al. Microbiologically influenced corrosion of FeCoCrNiMo_{0.1} high-entropy alloys by marine *Pseudomonas aeruginosa*. *Corros. Sci.* **165**, 108390 (2020).
50. Zhou, E. et al. A novel Cu-bearing high-entropy alloy with significant antibacterial behavior against corrosive marine biofilms. *J. Mater. Sci. Technol.* **46**, 201–210 (2020).
51. Jia, R. et al. Effects of biogenic H₂S on the microbiologically influenced corrosion of C1018 carbon steel by sulfate reducing *Desulfovibrio vulgaris* biofilm. *Corros. Sci.* **130**, 1–11 (2018).
52. Lou, Y. et al. Antibacterial ability of a novel Cu-bearing 2205 duplex stainless steel against *Pseudomonas aeruginosa* biofilm in artificial seawater. *Int Biodeterior. Biodegrad.* **110**, 199–205 (2016).
53. Qian, H. et al. Accelerating effect of catalase on microbiologically influenced corrosion of 304 stainless steel by the halophilic archaeon *Natronorubrum tibetense*. *Corros. Sci.* **178**, 109057 (2021).
54. Huang, Y. et al. Triple-action self-healing protective coatings based on shape memory polymers containing dual-function microspheres. *ACS Appl. Mater. Interfaces* **10**, 23369–23379 (2018).
55. Qian, H. et al. Laboratory investigation of microbiologically influenced corrosion of Q235 carbon steel by halophilic archaea *Natronorubrum tibetense*. *Corros. Sci.* **145**, 151–161 (2018).
56. Tang, S. et al. Fabrication of calcium carbonate coated-stainless steel mesh for efficient oil-water separation via bacterially induced biomineralization technique. *Chem. Eng. J.* **405**, 126597 (2021).

ACKNOWLEDGEMENTS

The work is supported by the National Natural Science Foundation of China (No. 52071015) and Fundamental Research Funds for the Central Universities (FRF-BD-20-28A2).

AUTHOR CONTRIBUTIONS

Yuntian Lou: investigation, methodology, and writing—original draft. Weiwei Chang: investigation and methodology. Tianyu Cui: investigation. Luyao Huang: investigation. Hongchang Qian: investigation. Lingwei Ma: investigation. Xiangping Hao: investigation. Dawei Zhang: supervision, conceptualization, methodology, and writing—original draft, writing—review and editing.

COMPETING INTERESTS

The authors declare no competing interests.

ADDITIONAL INFORMATION

Supplementary information The online version contains supplementary material available at <https://doi.org/10.1038/s41529-021-00206-0>.

Correspondence and requests for materials should be addressed to Dawei Zhang.

Reprints and permission information is available at <http://www.nature.com/reprints>

Publisher's note Springer Nature remains neutral with regard to jurisdictional claims in published maps and institutional affiliations.



Open Access This article is licensed under a Creative Commons Attribution 4.0 International License, which permits use, sharing, adaptation, distribution and reproduction in any medium or format, as long as you give appropriate credit to the original author(s) and the source, provide a link to the Creative Commons license, and indicate if changes were made. The images or other third party material in this article are included in the article's Creative Commons license, unless indicated otherwise in a credit line to the material. If material is not included in the article's Creative Commons license and your intended use is not permitted by statutory regulation or exceeds the permitted use, you will need to obtain permission directly from the copyright holder. To view a copy of this license, visit <http://creativecommons.org/licenses/by/4.0/>.

© The Author(s) 2021